



# Nanosecond pulsed laser irradiation induced hierarchical micro/nanostructures on Zr-based metallic glass substrate

Hu Huang<sup>a</sup>, Noguchi Jun<sup>a</sup>, Minqiang Jiang<sup>b</sup>, Moriya Ryoko<sup>a</sup>, Jiwang Yan<sup>a,\*</sup>

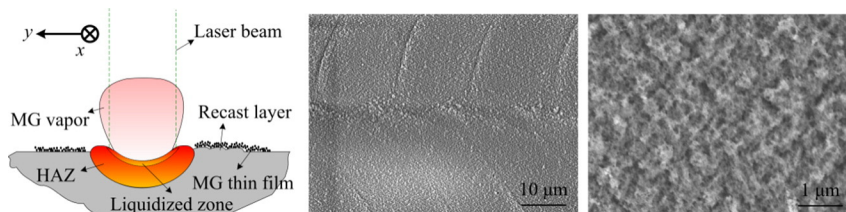
<sup>a</sup> Department of Mechanical Engineering, Faculty of Science and Technology, Keio University, Yokohama 223-8522, Japan

<sup>b</sup> State Key Laboratory of Nonlinear Mechanics, Institute of Mechanics, Chinese Academy of Sciences, Beijing 100190, People's Republic of China

## HIGHLIGHTS

- Hierarchical micro/nanostructures were fabricated on a metallic glass substrate by nanosecond pulsed laser irradiation.
- It retained amorphous characteristic and exhibited uniform element distribution.
- Irradiation parameters induced change from cotton-like to particle-like nanostructure.
- Formation mechanism and mechanical properties were investigated.

## GRAPHICAL ABSTRACT



## ARTICLE INFO

### Article history:

Received 19 March 2016

Received in revised form 17 June 2016

Accepted 12 July 2016

Available online 14 July 2016

### Keywords:

Hierarchical micro/nanostructure

Metallic glass

Thin film

Laser irradiation

Nanoindentation

## ABSTRACT

A large effective surface area is beneficial to enhance the applications of metallic glasses (MGs) in heterogeneous catalysis and biomedical engineering. For the purpose of increasing effective surface area, in this study, hierarchical micro/nanostructures were fabricated on a Zr-based MG substrate by nanosecond pulsed laser irradiation. Experimental results indicated that a layer of micron-scale laser pulse tracks covered by a cotton-like MG thin film with nanometer-scale microstructure was formed in the laser irradiated region. This hierarchical micro/nanostructures retained amorphous characteristic and exhibited uniform element distribution. Its formation mechanism was investigated by analyzing the laser irradiation process and morphologies. Nanoindentation results indicated that the cotton-like MG thin film was very loose and soft compared to the as-cast MG substrate, showing different plastic deformation behavior. Results from this study indicate that nanosecond pulsed laser irradiation is an effective method to generate hierarchical micro/nanostructures on MG substrates, which can increase their effective surface areas and improve their potential applications as biomaterials and catalysts.

© 2016 Elsevier Ltd. All rights reserved.

## 1. Introduction

Due to absence of dislocations and grain boundaries which are typically observed in crystalline materials, metallic glasses (MGs) without long-range topological order show excellent mechanical and chemical properties, such as high hardness and strength, large elastic limit as well as superior resistance to wear and corrosion [1–4]. These features make MGs to be regarded as very promising structural, engineering,

and sport materials [5,6]. Furthermore, MGs also show potentials in heterogeneous catalysis and biomedical engineering, but the featureless structure of the as-cast MGs significantly reduces their applicability in these fields because of small effective surface areas [7]. To solve this problem, introducing micro/nanostructures with enhanced effective surface areas into MGs is of great importance [7–9]. For example, via magnetron sputtering using mixed powders, Chen et al. [7] prepared a gold-based MG showing a heterogeneously granular structure with nanoparticles, which exhibited a high catalytic activity in the oxidation of organosilane compounds with water. By the same method, Zr–Pd MG thin films with a similar nanometer-scale surface structure were

\* Corresponding author.

E-mail address: [yan@mech.keio.ac.jp](mailto:yan@mech.keio.ac.jp) (J. Yan).

prepared by the same research group [8], which showed good biocompatibility for potential applications in biochemistry and implant engineering. Zhao et al. [9] used a chemical method to fabricate MG nanoparticles, which showed applications as highly durable catalysts in methanol electro-oxidation. However, these methods may be only suitable to certain kinds of MGs, and furthermore they are not economical or environmental-friendly [10,11]. Hence, new methods to generate micro/nanostructures on MG surfaces are greatly desired for their wide applications.

Although mechanical machining, typically diamond cutting [12–14], has been widely used to fabricate micro/nanostructures on the surface of soft metals because of its flexibility, such as copper by tuning tool paths [15], it may be not suitable for MGs. The high hardness of MGs (usually 6–8 times of copper) accelerates the tool wear which affects the uniformity and accuracy of the cutting surface [16,17]. For some hard-brittle MGs, mechanical machining becomes more difficult. For example, most of Fe-based MGs show high hardness (~12 GPa) but very low fracture toughness (~10 MPa m<sup>1/2</sup>) [18], although some Fe-based MGs with enhanced ductility had been reported recently [19]. Furthermore, very low thermal conductivity of MGs results in a high local temperature in the cutting region especially during high speed cutting. Thus, oxidation and crystallization of MGs may occur [20] which probably affect their amorphous performances [21,22], but this kind of effects is dependent of the properties and volume fraction of the crystalline phases [21–23] as well as the sample preparation and evaluation methods [24,25]. In addition, high local temperature will also increase the adhesion between the chip and tool, leading to the formation of built-up edge on the rake face, and thus affect the subsequent cutting process [16,26]. Hence, fabrication of micro/nanostructured surfaces on MGs by mechanical machining is challenging.

Taking the feature of viscous state in the supercooled temperature region (between the glass transition and crystallization temperature), thermoplastic shaping was reported to form micro/nanostructured surfaces on MGs [27–29]. However, the high cost to fabricate the micro/nanostructured molds as well as the limited mold-life-times hinders its wide applications [2]. Furthermore, crystallization may also occur during the thermoplastic shaping because it is very hard to control a uniform forming temperature [30], especially for MGs with a narrow supercooled temperature region.

In recent years, nanosecond pulsed laser irradiation was adopted to fabricate micro/nanostructured surfaces that possess unique optical, photoelectric, catalytic, mechanical, and wetting properties. For example, superhydrophobic surfaces were obtained by nanosecond laser texturing or ablation [31]. Via nanosecond laser ablation, micro/nanostructures were patterned on silicon surface [32], resulting in decreased reflectivity, which has potential applications in solar cells. For MGs, previous studies by nanosecond pulsed laser irradiation with a single shot showed that surface ripple patterns as well as porous structure consisting of 100 nm-scale voids were formed in the irradiated area [33–35]. However, large-area nanosecond pulsed laser irradiation of MG surfaces has been rarely investigated, but it has the potential to generate hierarchical micro/nanostructured surfaces with enhanced effective surface areas according to the following considerations. Firstly, during single pulsed laser shot, a micro-crater can be formed. If line irradiation is implemented along two directions with an overlapped region between two craters, a layer of laser pulse tracks can be patterned on MGs. Secondly, when the laser intensity is sufficiently high, the irradiated materials may experience phase changes, vaporization, boiling, and even explosive boiling, accompanying with the ejection of a high-temperature matter because of the recoil pressure [34–38]. By re-deposition of the vapor particles in the adjacent irradiated region, a layer of MG thin film is expected to be formed over the first layer of laser pulse tracks. According to aforementioned analysis, we attempt to fabricate hierarchical micro/nanostructured surfaces on a MG substrate via nanosecond pulsed laser irradiation in this study, and further discuss its formation mechanism as well as mechanical properties.

## 2. Experimental procedure

Zr<sub>41.2</sub>Ti<sub>13.8</sub>Cu<sub>12.5</sub>Ni<sub>10</sub>Be<sub>22.5</sub> MG sample (commonly called Vitreloy 1 [39]) with a diameter of 10 mm and thickness of 2 mm was used. Before laser irradiation, it was mechanically polished using 400, 800, and 1500 grit sand papers in sequence. A Nd:YAG nanosecond pulsed laser system (LR-SHG, MegaOpto Co., Ltd., Japan) with a wavelength of 532 nm and a pulse width of 15.4 ns was used. The laser beam was shaped to a square section of ~85 μm × 85 μm. The pulse frequency was kept 1 kHz, and the overlapped region between two scanning lines was 45 μm. Various scanning speeds, 1, 5, and 10 mm/s, were used during laser irradiation, which theoretically resulted in various overlapped regions along a scanning line, 84, 80, and 75 μm, respectively. Also various average laser powers (0.013–0.649 W) were used, corresponding to peak laser powers in the range of 8.4 × 10<sup>2</sup>–4.2 × 10<sup>4</sup> W. According to Ref. [40], the peak laser power intensity was calculated to be in the range of 1.2 × 10<sup>11</sup>–5.8 × 10<sup>12</sup> W/m<sup>2</sup>. To avoid oxidation, vacuum environment was realized by 5 min vacuum pumping of the sample chamber (65 mm × 65 mm × 45 mm) before laser irradiation.

Microstructures of the MG after laser irradiation were observed by a three dimensional (3D) laser scanning microscope (VK-9700, Keyence, Japan) and a field emission scanning electron microscope (FE-SEM) (JSM-7600F, JEOL, Japan). An X-ray diffractometer (XRD, D8 Discover, Bruker, Germany) was used to characterize the amorphous characteristic of the MG before and after laser irradiation. Element mapping was performed on the irradiated region by an energy dispersive X-ray spectroscopy (EDX, XFlash Detector 4010, Bruker, Germany). Nanoindentation tests were performed on an ENT-1100 nanoindentation instrument (Elionix Inc., Japan) equipped with a Berkovich type diamond indenter, and their residual morphologies were also observed by the FE-SEM.

## 3. Results and discussion

### 3.1. Morphological analysis

Fig. 1 presents representative optical morphologies of the laser irradiated region under an average power of 0.402 W and scanning speed of 10 mm/s. Under this condition, the peak laser power and power intensity was 2.6 × 10<sup>4</sup> W and 3.6 × 10<sup>12</sup> W/m<sup>2</sup>, respectively, and the laser fluence was 5.6 J/cm<sup>2</sup>. In Fig. 1(a), a rectangle irradiated region was formed on the MG surface. Laser irradiation started from the upper-right corner and ended at the bottom-right corner. Fig. 1(b) gives the local enlarged view of Fig. 1(a), where many remarkable laser pulse tracks are observed. The reversed direction between two adjacent scanning lines results from reversed laser scanning direction. Fig. 1(c) shows the 3D morphology corresponding to Fig. 1(b), and Fig. 1(d) and (e) show the profiles along the solid line and dashed line in Fig. 1(b), respectively. The height of laser pulse tracks periodically varies in micron-scale in both x and y directions. The curved surface can effectively increase the surface area. For example, the measurement result by the 3D laser scanning microscope indicates that the effective surface area for the evaluated region in Fig. 1(c) is 1.57 times of the corresponding flat surface area. From Fig. 1, it can be concluded that a layer of laser pulse tracks in micron-scale has been successfully formed in the irradiated region. It should be noted that the microstructure and height shown in Fig. 1 can be tuned easily by changing the laser scanning speed, power and overlapped region, resulting in various effective surface areas.

Because the optical microscope had a limited magnification, FE-SEM was used to further observe the detailed microstructure in the irradiated region shown in Fig. 1 with higher magnifications, and results are presented in Fig. 2. In Fig. 2(a), the irradiated region (region 1) is surrounded by a grey region (region 2) with a width of ~370 μm, which is the heat affected zone (HAZ). Fig. 2(b), (c), and (d) are the local enlarged views of the region 1, and Fig. 2(e) and (f) are the local

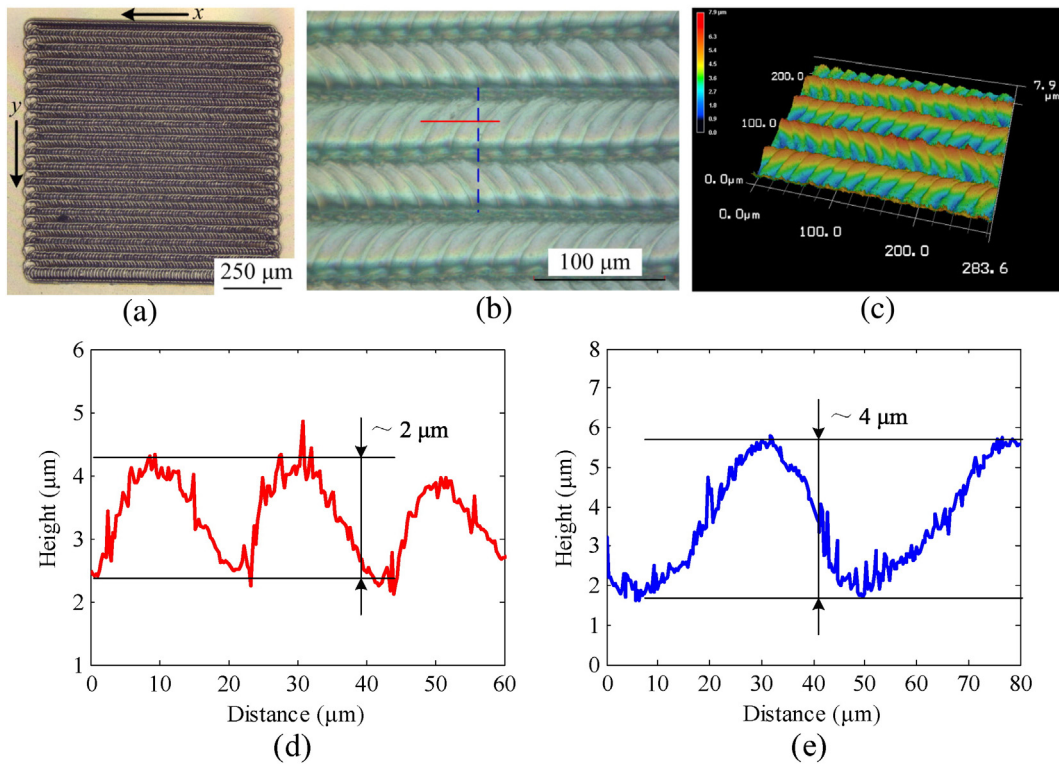


**Fig. 1.** (a) Optical morphology of the laser irradiated region under a power of 0.402 W and scanning speed of 10 mm/s. (b) Local enlarged view of Fig. 1(a) showing the microstructure in detail. (c) 3D morphology corresponding to Fig. 1(b). (d) and (e) show the profiles along the solid line and dashed line in Fig. 1(b), respectively.

enlarged views of the region 2. Apart from the individual laser pulse tracks which have been observed in Fig. 1, a cotton-like film with nanometer-scale microstructure is uniformly distributed on the top surface of each pulse track in region 1. Similarly, this cotton-like film was also formed in region 2 although no direct laser irradiation was performed in this region. Accordingly, hierarchical micro/nanostructures, micron-scale laser pulse tracks covered by a cotton-like film with nanometer-scale microstructure, are confirmed that have formed in the laser irradiated region.

To further confirm that hierarchical micro/nanostructures can be formed under various laser irradiation parameters, laser irradiations were performed on the MG surface under various parameters. Fig. 3 presents representative FE-SEM morphologies under a higher average power of 0.649 W (Fig. 3(a)–(c)) and a lower scanning speed of 1 mm/s (Fig. 3(d)–(f)). Other parameters for Fig. 3 are the same to those for Figs. 1 and 2. It can be seen that hierarchical micro/nanostructures were also generated for these two parameters. In Fig. 3(a)–3(c), laser pulse tracks with more remarkable wrinkle appear compared to

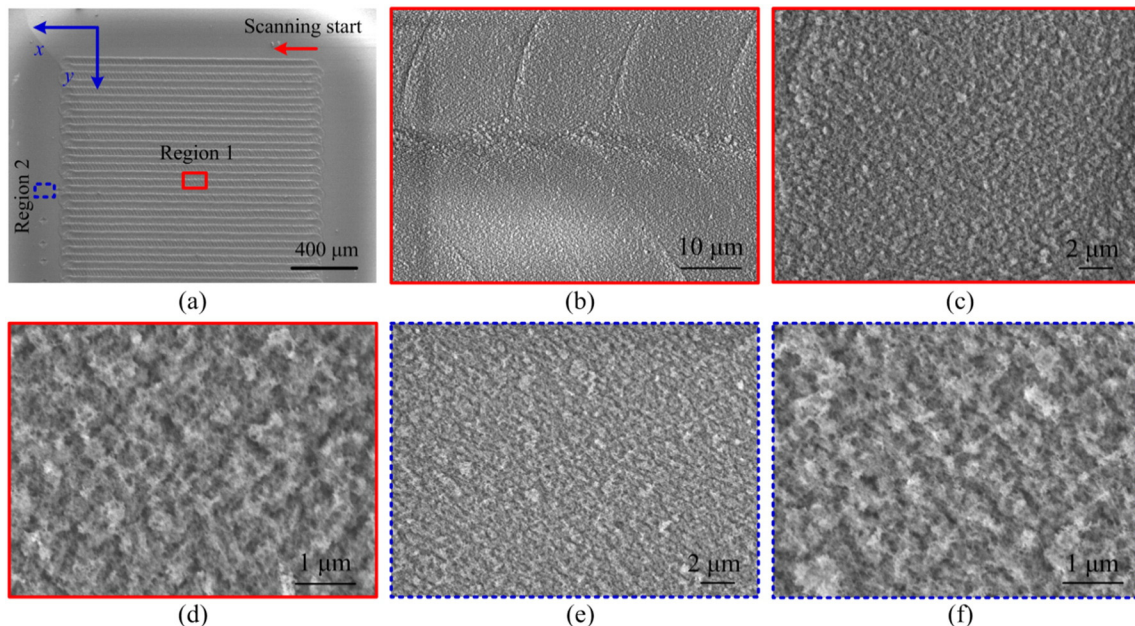


**Fig. 2.** FE-SEM morphologies of the laser irradiated surface at different regions and magnifications.

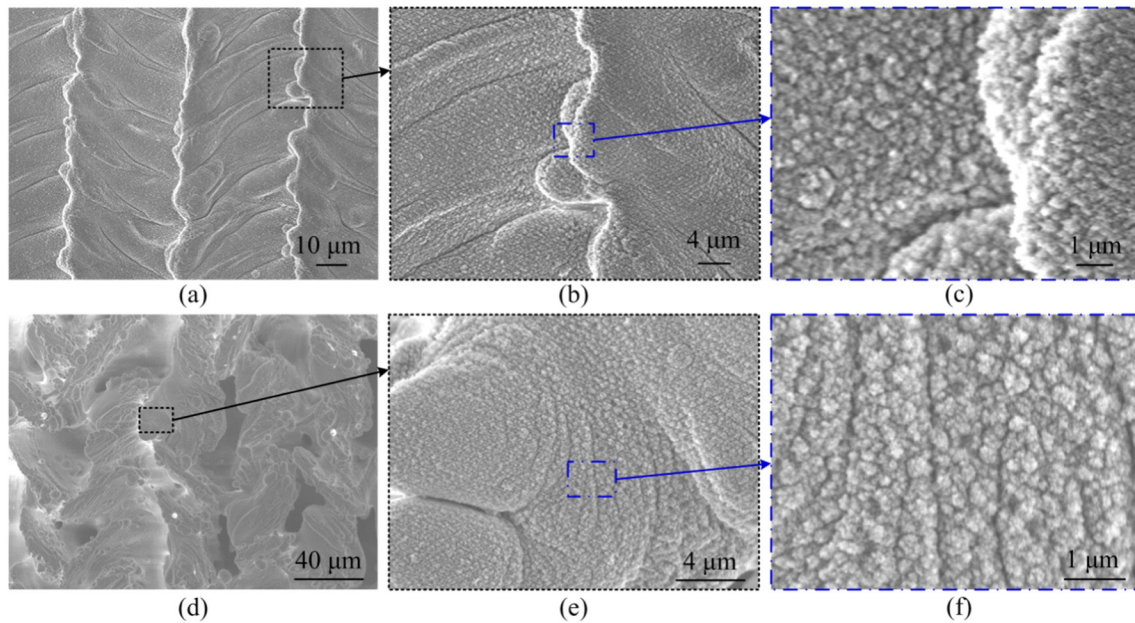


**Fig. 3.** FE-SEM morphologies under various laser irradiation parameters. Fig. 3(a)–(c) are morphologies under a higher average power of 0.649 W, and Fig. 3(d)–(f) are morphologies under a lower scanning speed of 1 mm/s. Other parameters for Fig. 3 are the same to those for Figs. 1 and 2.

those in Fig. 2(b). With the increase of the laser power, more materials were heated during a single shot, and the recoil pressure may be also enhanced. Thus, more materials were pushed to flow outside the crater, leading to more remarkable wrinkle. In Fig. 3(d), laser pulse tracks become non-uniform. In this case, although the laser power for a single shot is the same to that in Fig. 2, more laser shots were applied for the same irradiated region because of the low laser scanning speed, resulting in an increased overlapped region (84  $\mu\text{m}$ ) along a scanning line. Therefore, more heat was accumulated in a single shot region, leading to the irregular laser pulse tracks in Fig. 3(d). Furthermore, instead of the cotton-like nanostructure in Fig. 2(d) and (f), particle-like nanostructures as shown in Fig. 3(c) and (f) were formed on the surface of laser pulse tracks, demonstrating that more materials were ejected in these two cases because of the increased laser power and decreased scanning speed. The change in hierarchical micro/nanostructures also leads to various effective surface areas. Corresponding to the morphologies in Fig. 3(a) and (d), the effective surface areas measured by the 3D laser scanning microscope are 5.1 and 24.3 times of the flat surface area.

### 3.2. XRD and EDX analysis

Fig. 4(a) presents the XRD patterns of the regions 1 and 2 in Fig. 2(a) as well as the as-cast MG surface. Compared to the as-cast sample surface, both the laser irradiated region and the HAZ (non-irradiated region) show the amorphous characteristic, and no crystallization peaks appear in these two regions. It should be noted that for the irradiation parameters corresponding to Fig. 3, the irradiated surfaces also show an amorphous characteristic (results are not given here). The remained amorphous characteristic results from both high heating and cooling rates during nanosecond pulsed laser irradiation, which is higher than the critical value of the crystallization of Vitreloy 1 [41]. Combining the results in Figs. 1, 2 and 3(a), the laser irradiated regions on the MG surface exhibit the hierarchical micro/nanostructures and meanwhile retain the amorphous characteristic.

Fig. 4(b)–(g) give the results of EDX element mappings measured in the region 1. Be element was not detected, because it is a light chemical element and its measurement by the EDX system may be not reliable. From Fig. 4(b)–(g), it is noted that Zr, Ti, Cu, and Ni elements are distributed uniformly in the irradiated region, indicating that laser irradiation

under current experimental conditions does not result in phase separation or element enrichment.

### 3.3. Formation mechanism of the hierarchical micro/nanostructures

Previous studies [34–36,42] indicated that during nanosecond pulsed laser irradiation, the irradiated materials may experience heating, melting, vaporization, boiling, and even explosive boiling, and these processes were determined by the laser intensity, fluence, peak power, pulse width, wavelength as well as material properties. For a single pulsed laser irradiation with a wavelength of 1064 nm, pulse width of 10 ns and fluence of 11 J/cm<sup>2</sup> corresponding to a laser intensity of  $1.1 \times 10^{13}$  W/m<sup>2</sup>, explosive boiling of Vitreloy 1 MG accompanying with a violent ejection of high-temperature mixture of vapor and droplets was reported [34]. While, for a single pulsed laser irradiation with a wavelength of 1064 nm, pulse width of 15 ns and fluence of 7.6 J/cm<sup>2</sup> corresponding to a laser intensity of  $5.1 \times 10^{12}$  W/m<sup>2</sup>, normal vaporization of Vitreloy 1 MG was derived [35]. Because the laser intensity used here is in the magnitude order of  $10^{12}$  W/m<sup>2</sup>, which is an order of magnitude lower than that in Ref. [34] (corresponding to explosive boiling) and is similar to that in Ref. [35] (normal vaporization), and thus, it is derived that the Vitreloy 1 MG experienced heating, liquidizing, and normal vaporization for the case in this study.

To further understand the laser irradiation process and explore the formation mechanism of the hierarchical micro/nanostructures, the surface temperature and surface vapor pressure changing with the time during a single pulsed laser irradiation were predicted by using the thermal model proposed in Ref. [34], and Fig. 5(a) presents the calculation results under the laser intensity of  $3.6 \times 10^{12}$  W/m<sup>2</sup> and fluence of 5.6 J/cm<sup>2</sup>, where  $T_b$  is the boiling temperature at standard atmospheric pressure  $p_b$ ,  $\sim 3792$  K for Vitreloy 1 calculated by atomic mole ratio [34]. The surface temperature gradually increases with the time increasing, and at 18.4 ns, it is over the boiling point  $T_b$ . At 26.4 ns, the surface temperature reaches the maximum value of 4481 K, which is 0.62 time of the thermodynamic critical point  $T_c$  ( $\sim 7196$  K for Vitreloy 1 calculated by the empirical equation proposed in Refs. [38,43]) [34]. For explosive boiling of Vitreloy 1, the maximum temperature is required to be  $\sim 0.83 T_c$  [34]. Hence, only normal vaporization occurred here. Corresponding to the maximum surface temperature, a maximum surface vapor pressure of 181  $p_b$  is obtained, which is close to the saturation vapor

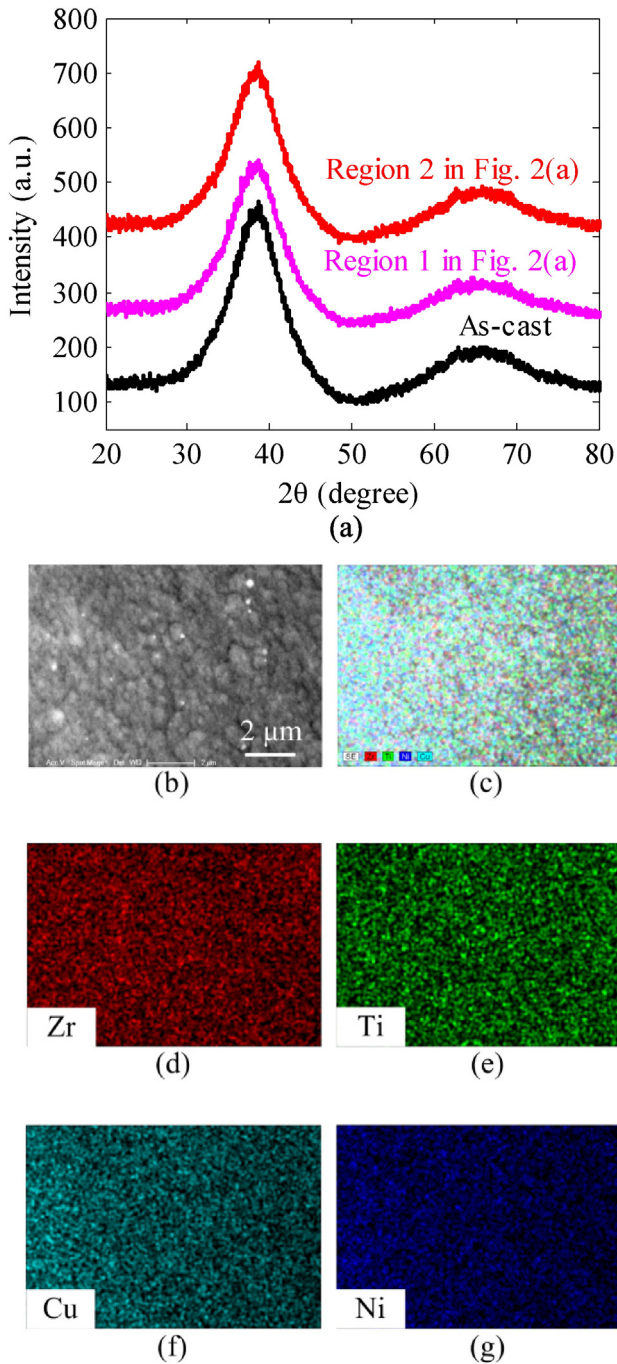


**Fig. 4.** (a) XRD patterns of the MG before and after laser irradiation. (b) Measurement region of EDX element mappings. Results of EDX element mappings: (c) Zr, Ti, Cu, and Ni, (d) Zr, (e) Ti, (f) Cu, and (g) Ni.

pressure. This further confirms that explosive boiling had not happened, because explosive boiling will reduce the maximum surface vapor pressure to be much lower than the saturation vapor pressure [34,38].

Accordingly, the possible formation mechanism of the hierarchical micro/nanostructures is illustrated in Fig. 5(b). Laser energy is absorbed by the MG, causing very fast temperature raise of the irradiated region. For the line irradiation here, residual heat in previous irradiation also contributes to the fast temperature raise of subsequent irradiation especially for a low scanning speed. In the center region, some materials are liquidized. Compared to femtosecond pulsed laser, nanosecond pulsed laser has a relatively long duration and thus a large HAZ is formed underneath the liquidized materials as well as on the top surface. Materials in the liquidized zone and HAZ have enhanced flow. With the role of the

recoil pressure generated by vaporization, some liquidized materials and some materials in HAZ are pushed towards the edge of the crater, forming the laser pulse tracks. On the other hand, some materials in the center region are vaporized as very fine vapor particles. As time goes on, the vaporized materials are cooled, and then deposited and re-solidified on the surface of the adjacent irradiated regions as well as un-irradiated regions. With accumulation of the deposited materials particle by particle and layer by layer, a MG thin film with nanostructures as shown in Figs. 2(d), (f), 3(c), and (f) is formed on the top surface of the irradiated region as well as the surrounded HAZ. The MG thin film with nanostructures formed in the HAZ provides a believable evidence for aforementioned formation mechanism.

To further confirm this mechanism, morphologies of the last one and the penultimate scanning lines in Fig. 1(a) were observed. Fig. 6(a) shows FE-SEM morphology of the last irradiated line at the scanning end. A HAZ with a width of 10  $\mu\text{m}$  was formed around the last scanning line. Compared to Fig. 2(b), more remarkable laser pulse tracks are observed in Fig. 6(a), but no cotton-like nanostructure similar to those in Fig. 2(b)–(d) appears. Fig. 6(b) presents the local enlarged view of the solid rectangle region in Fig. 6(a), where some nanoparticles had been deposited. For a single pulsed laser irradiation [35], some nanoparticles also appeared on the irradiated surface under a pulse width of 15 ns and power intensity of  $5.1 \times 10^{12} \text{ W/m}^2$ . These results further confirm the vaporization and re-deposition mechanism mentioned above. Furthermore, Fig. 6(c) and (d) show the FE-SEM morphologies of the dashed rectangle region in Fig. 6(a), i.e., the penultimate scanning line in Fig. 1(a). Being different from the last one, the cotton-like film with nanostructures has generated on the surface of the penultimate scanning line. However, the nanostructure on the penultimate scanning line in Fig. 6(d) has a little larger size than those in Fig. 2(d) and (f) because of only one time deposition. These differences in nanostructure between the center region (region 1), the last one and the penultimate further confirm that the cotton-like film observed in region 1 was formed particle by particle and layer by layer by subsequent deposition and re-solidification of the vaporized materials during the adjacent laser irradiation processes. In addition, subsequent laser scanning processes lower previous laser pulse tracks and reduce the nanostructure size because of the heating and cooling processes as well as the gradually deposited MG film. The reason for the structure change from cotton-like nanostructure in Fig. 2(d) and (f) to particle-like nanostructure in Fig. 3(c) and (f) is that more materials were vaporized under the increased laser power and decreased scanning speed, and the cotton-like nanostructure may grow and self-assemble to form the particle-like nanostructure accompanying with further deposition.

### 3.4. Nanoindentation analysis

To characterize the mechanical properties of the deposited MG thin film with a cotton-like structure, the nanoindentation method was used. Because the irradiated surface was not flat, nanoindentation experiments were carried out on the surface of HAZ as shown in Fig. 2(a) under a maximum indentation load of 10 mN and loading/unloading rate of 0.5 mN/s. For comparison, nanoindentation experiments were also performed on the as-cast MG surface. The nanoindentation curves and residual morphologies are presented in Fig. 7 and Fig. 8, respectively.

In Fig. 7(a) and (b), it is noted that for the same indentation load of 10 mN, the maximum indentation depth for the surface of HAZ with the MG thin film is 1088 nm, which is significantly larger than that for the as-cast MG surface (243 nm). Furthermore, the loading portion in Fig. 7(b) shows two stages. In the depth of 0–800 nm, the indentation load very slowly increases, and at the depth of 800 nm, the indentation load is still less than 1 mN. When the indenter penetrates more than 800 nm, the indentation load increases quickly, just like the loading portion in Fig. 7(a). Corresponding to these two stages, two layers, MG thin film and MG substrate, can also be easily distinguished in the residual



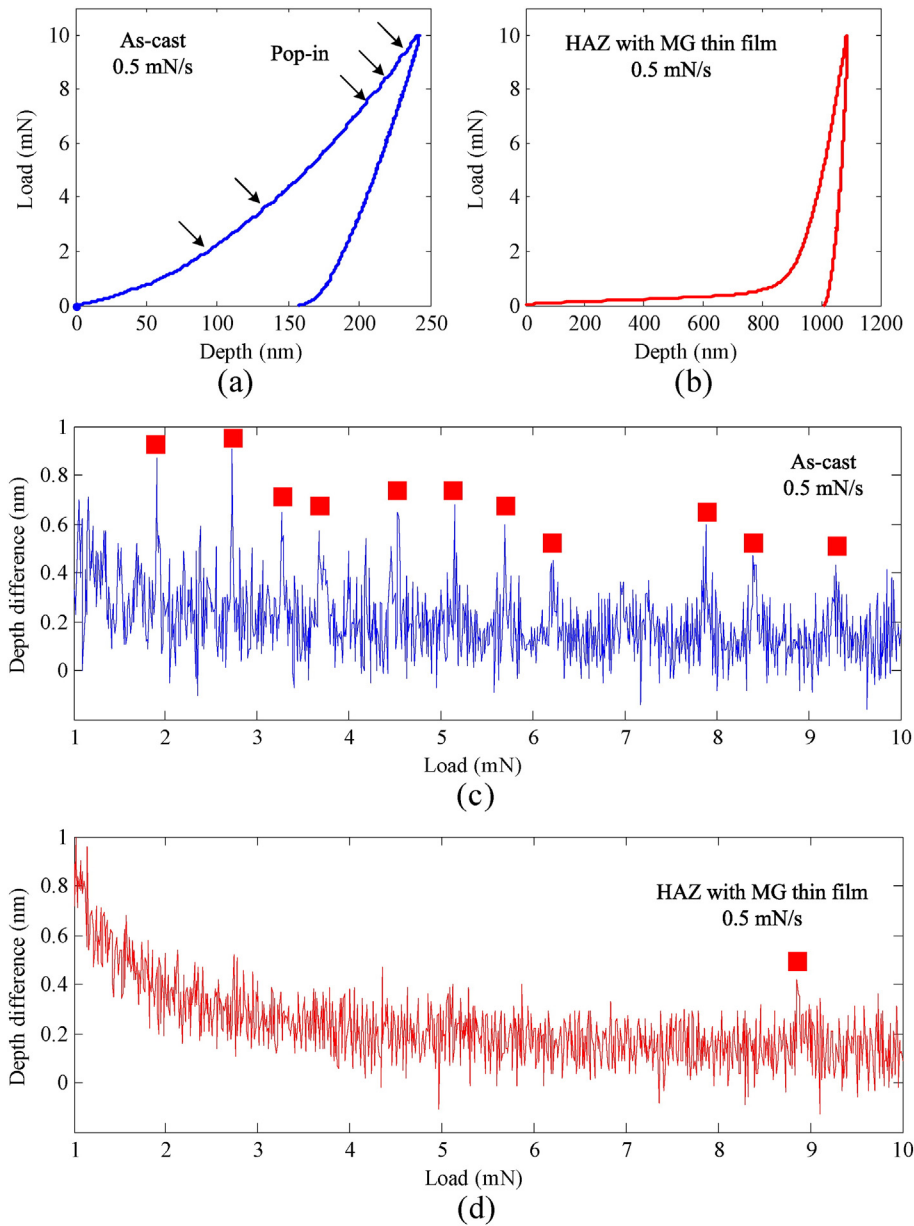


**Fig. 7.** Load-depth curves obtained on (a) the as-cast MG surface and (b) the surface of HAZ with the MG thin film. Fig. 7(c) and (d) show the depth difference changing with the indentation load corresponding to Fig. 7(a) and (b), respectively.

changing with the indentation loads are illustrated in Fig. 7(c) and (d), corresponding to the load-depth curves in Fig. 7(a) and (b) respectively. In Fig. 7(c), there are many sharp peaks, while only one weak peak is observed in Fig. 7(d) at the indentation load of ~9 mN. According to the depth difference method [47], a pop-in results in a sharp peak in the depth difference-load curve. Hence, it is confirmed that the load-depth curve in Fig. 7(b) has very few pop-ins. Previous studies suggested two mechanisms for explaining the pop-ins. One is operations of shear bands including initiation, propagation and arrest [44], and the other is related to the elastic-plastic transition of MGs [48]. Both of these two mechanisms are related to the plastic deformation process of MGs. The difference in pop-in implies different plastic deformation process of the MG thin film, compared to that of the MG substrate. As shown in Figs. 2, 8(a) and (b), the cotton-like MG thin film can easily accommodate the strain applied by the indenter, resulting in a large and continuous depth change. When the indenter penetrates through the MG thin film and contacts the MG substrate, the intrinsic high-hardness of the MG substrate leads to fast increase in indentation load for a small

depth change. Meanwhile, pop-in may also appear as shown in Fig. 7(d) because of penetration into MG substrate. The slow load increase yielding a large depth change in Fig. 7(b) as well as the residual indentation morphologies in Fig. 8(a) and (b) further confirms the cotton-like loose structure of the MG thin film in Fig. 2, which can effectively increase the effective surface area.

#### 4. Conclusions

Nanosecond pulsed laser irradiation has been used to fabricate hierarchical micro/nanostructures on a MG substrate. The resulting surface consists of two layers, a layer of micron-scale laser pulse tracks covered by a cotton-like MG thin film with nanometer-scale microstructure. XRD patterns confirmed that this hierarchical micro/nanostructure retained an amorphous characteristic, and EDX mappings demonstrated that elements of the MG thin film were distributed uniformly. Morphological analysis showed that the MG thin film was formed through deposition and re-solidification of the vaporized materials during the

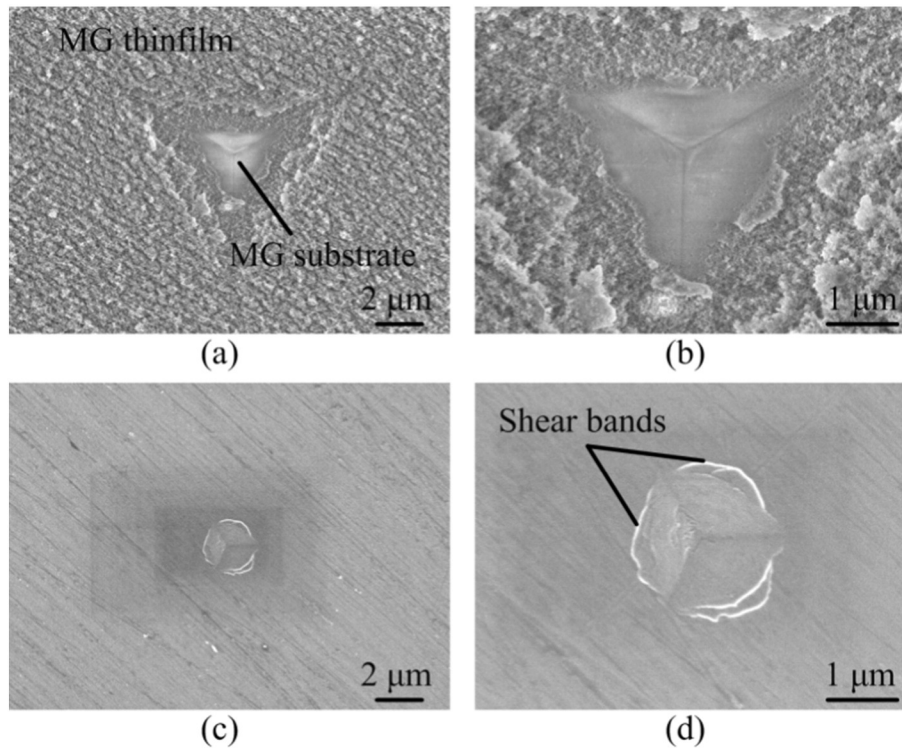


**Fig. 8.** Residual nanoindentation morphologies: (a) and (b) are morphologies corresponding to the nanoindentation curve in Fig. 7(b), and (c) and (d) are morphologies corresponding to the nanoindentation curve in Fig. 7(a).

adjacent laser irradiation. When the laser power was increased or the scanning speed was decreased, the MG thin film transformed from the cotton-like nanostructure to a particle-like nanostructure. Nanoindentation results further confirmed that the cotton-like MG thin film was very loose and soft compared to the MG substrate, having very different plastic deformation behavior. The hierarchical micro/nanostructures produced by nanosecond pulsed laser irradiation show increased effective surface areas, which are useful for improving the applications of MGs as biomaterials and catalysts.

### Acknowledgments

H.H. is an International Research Fellow of the Japan Society for the Promotion of Science (JSPS). This study has been financially supported by Grant-in-Aid for JSPS Fellows (Grant No. 26-04048).

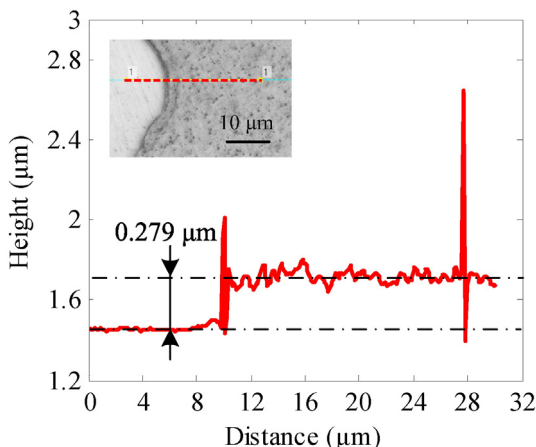


**Fig. 9.** Thickness of the MG thin film measured near the indent in the HAZ.

### References

- [1] M.M. Trexler, N.N. Thadhani, Mechanical properties of bulk metallic glasses, *Prog. Mater. Sci.* 55 (2010) 759–839.
- [2] J. Plummer, W.L. Johnson, Is metallic glass poised to come of age? *Nat. Mater.* 14 (2015) 553–555.
- [3] C.J. Byrne, M. Eldrup, Materials science – bulk metallic glasses, *Science* 321 (2008) 502–503.
- [4] W.H. Wang, The elastic properties, elastic models and elastic perspectives of metallic glasses, *Prog. Mater. Sci.* 57 (2012) 487–656.
- [5] A. Inoue, A. Takeuchi, Recent development and applications of bulk glassy alloys, *Int. J. Appl. Glas. Sci.* 1 (2010) 273–295.
- [6] N.W. Khun, H. Yu, Z.Z. Chong, P. Tian, Y. Tian, S.B. Tor, E. Liu, Mechanical and tribological properties of Zr-based bulk metallic glass for sports applications, *Mater. Des.* 92 (2016) 667–673.
- [7] N. Chen, R. Frank, N. Asao, D.V. Louzguine-Luzgin, P. Sharma, J.Q. Wang, G.Q. Xie, Y. Ishikawa, N. Hatakeyama, Y.C. Lin, M. Esashi, Y. Yamamoto, A. Inoue, Formation and properties of Au-based nanograined metallic glasses, *Acta Mater.* 59 (2011) 6433–6440.
- [8] S.V. Ketov, X.T. Shi, G.Q. Xie, R. Kumashiro, A.Y. Churyumov, A.I. Bazlov, N. Chen, Y. Ishikawa, N. Asao, H.K. Wu, D.V. Louzguine-Luzgin, Nanostructured Zr–Pd metallic glass thin film for biochemical applications, *Sci. Rep. Uk* 5 (2015) 7799.
- [9] M. Zhao, K. Abe, S. Yamaura, Y. Yamamoto, N. Asao, Fabrication of Pd–Ni–P metallic glass nanoparticles and their application as highly durable catalysts in methanol electro-oxidation, *Chem. Mater.* 26 (2014) 1056–1061.
- [10] H. Gleiter, Nanoglasses: a new kind of noncrystalline materials, *Beilstein J. Nanotech.* 4 (2013) 517–533.
- [11] H. Gleiter, T. Schimmel, H. Hahn, Nanostructured solids – from nano-glasses to quantum transistors, *Nano Today* 9 (2014) 17–68.
- [12] E. Brinksmeier, O. Riemer, R. Glabe, B. Lunemann, C. von Kopylow, C. Dankwart, A. Meier, Submicron functional surfaces generated by diamond machining, *CIRP Ann. Manuf. Techn.* 59 (2010) 535–538.
- [13] S.L. Xu, K. Shimada, M. Mizutani, T. Kuriyagawa, Fabrication of hybrid micro/nano-textured surfaces using rotary ultrasonic machining with one-point diamond tool, *Int. J. Mach. Tool. Manu.* 86 (2014) 12–17.
- [14] P. Guo, Y. Lu, K.F. Ehmman, J. Cao, Generation of hierarchical micro-structures for anisotropic wetting by elliptical vibration cutting, *CIRP Ann. Manuf. Techn.* 63 (2014) 553–556.
- [15] Z.W. Zhu, S. To, S.J. Zhang, Theoretical and experimental investigation on the novel end-fly-cutting-servo diamond machining of hierarchical micro-nanostructures, *Int. J. Mach. Tool. Manu.* 94 (2015) 15–25.
- [16] M. Bakka, A.J. Shih, R.O. Scattergood, Chip formation, cutting forces, and tool wear in turning of Zr-based bulk metallic glass, *Int. J. Mach. Tool. Manu.* 44 (2004) 915–925.
- [17] K. Fujita, Y. Morishita, N. Nishiyama, H. Kimura, A. Inoue, Cutting characteristics of bulk metallic glass, *Mater. Trans.* 46 (2005) 2856–2863.

- [18] J.J. Lewandowski, W.H. Wang, A.L. Greer, Intrinsic plasticity or brittleness of metallic glasses, *Phil. Mag. Lett.* 85 (2005) 77–87.
- [19] S.F. Guo, J.L. Qiu, P. Yu, S.H. Xie, W. Chen, Fe-based bulk metallic glasses: brittle or ductile? *Appl. Phys. Lett.* 105 (2014) 161901.
- [20] M. Bakkal, C.T. Liu, T.R. Watkins, R.O. Scattergood, A.J. Shih, Oxidation and crystallization of Zr-based bulk metallic glass due to machining, *Intermetallics* 12 (2004) 195–204.
- [21] C.J. Gilbert, R.O. Ritchie, W.L. Johnson, Fracture toughness and fatigue-crack propagation in a Zr–Ti–Ni–Cu–Be bulk metallic glass, *Appl. Phys. Lett.* 71 (1997) 476–478.
- [22] N. Nagendra, U. Ramamurty, T.T. Goh, Y. Li, Effect of crystallinity on the impact toughness of a La-based bulk metallic glass, *Acta Mater.* 48 (2000) 2603–2615.
- [23] J. Ketkaew, Z. Liu, W. Chen, J. Schroers, Critical crystallization for embrittlement in metallic glasses, *Phys. Rev. Lett.* 115 (2015) 265502.
- [24] W. Chen, J. Ketkaew, Z. Liu, R.M.O. Mota, K. O'Brien, C.S. da Silva, J. Schroers, Does the fracture toughness of bulk metallic glasses scatter? *Scripta Mater.* 107 (2015) 1–4.
- [25] W. Chen, Z. Liu, J. Ketkaew, R.M.O. Mota, S.H. Kim, M. Power, W. Samela, J. Schroers, Flaw tolerance of metallic glasses, *Acta Mater.* 107 (2016) 220–228.
- [26] H. Huang, H.W. Zhao, C.L. Shi, B.D. Wu, Z.Q. Fan, S.G. Wan, C.Y. Geng, Effect of residual chips on the material removal process of the bulk metallic glass studied by in situ scratch testing inside the scanning electron microscope, *AIP Adv.* 2 (2012) 042193.
- [27] G. Kumar, H.X. Tang, J. Schroers, Nanomoulding with amorphous metals, *Nature* 457 (2009) 868–872.
- [28] Z. Hu, S. Gorumlu, B. Aksak, G. Kumar, Patterning of metallic glasses using polymer templates, *Scripta Mater.* 108 (2015) 15–18.
- [29] P. He, L.K. Li, F. Wang, O. Dambon, F. Klocke, K.M. Flores, A.Y. Yi, Bulk metallic glass mold for high volume fabrication of micro optics, *Microsyst. Technol.* 22 (2016) 617–623.
- [30] G. Kaltenboeck, T. Harris, K. Sun, T. Tran, G. Chang, J.P. Schramm, M.D. Demetriou, W.L. Johnson, Accessing thermoplastic processing windows in metallic glasses using rapid capacitive discharge, *Sci. Rep. UK* 4 (2014) 6441.
- [31] D.V. Ta, A. Dunn, T.J. Wasley, R.W. Kay, J. Stringer, P.J. Smith, C. Connaughton, J.D. Shephard, Nanosecond laser textured superhydrophobic metallic surfaces and their chemical sensing applications, *Appl. Surf. Sci.* 357 (2015) 248–254.
- [32] J. Yang, F.F. Luo, T.S. Kao, X. Li, G.W. Ho, J.H. Teng, X.G. Luo, M.H. Hong, Design and fabrication of broadband ultralow reflectivity black Si surfaces by laser micro/nanoprocessing, *Light-Sci. Appl.* 3 (2014), e185.
- [33] Y. Liu, M.Q. Jiang, G.W. Yang, Y.J. Guan, L.H. Dai, Surface rippling on bulk metallic glass under nanosecond pulse laser ablation, *Appl. Phys. Lett.* 99 (2011) 191902.
- [34] M.Q. Jiang, Y.P. Wei, G. Wilde, L.H. Dai, Explosive boiling of a metallic glass superheated by nanosecond pulse laser ablation, *Appl. Phys. Lett.* 106 (2015) 021904.
- [35] E. Williams, E.B. Brousseau, Nanosecond laser processing of  $Zr_{41.2}Ti_{13.8}Cu_{12.5}Ni_{10}Be_{22.5}$  with single pulses, *J. Mater. Process. Tech.* 232 (2016) 34–42.
- [36] A. Miotello, R. Kelly, Critical-assessment of thermal models for laser sputtering at high fluences, *Appl. Phys. Lett.* 67 (1995) 3535–3537.
- [37] J.H. Yoo, S.H. Jeong, X.L. Mao, R. Greif, R.E. Russo, Evidence for phase-explosion and generation of large particles during high power nanosecond laser ablation of silicon, *Appl. Phys. Lett.* 76 (2000) 783–785.
- [38] N.M. Bulgakova, A.V. Bulgakov, Pulsed laser ablation of solids: transition from normal vaporization to phase explosion, *Appl. Phys. A Mater.* 73 (2001) 199–208.
- [39] A. Peker, W.L. Johnson, A highly processable metallic-glass —  $Zr_{41.2}Ti_{13.8}Cu_{12.5}Ni_{10}Be_{22.5}$ , *Appl. Phys. Lett.* 63 (1993) 2342–2344.
- [40] Y.B. Guo, R. Caslaru, Fabrication and characterization of micro dent arrays produced by laser shock peening on titanium Ti-6Al-4V surfaces, *J. Mater. Process. Tech.* 211 (2011) 729–736.
- [41] J. Schroers, A. Masuhr, W.L. Johnson, R. Busch, Pronounced asymmetry in the crystallization behavior during constant heating and cooling of a bulk metallic glass-forming liquid, *Phys. Rev. B* 60 (1999) 11855–11858.
- [42] C. Porneala, D.A. Willis, Time-resolved dynamics of nanosecond laser-induced phase explosion, *J. Phys. D: Appl. Phys.* 42 (2009) 155503.
- [43] M.M. Martynyuk, Critical constants of metals, *Russ. J. Phys. Chem.* 57 (1983) 494–501.
- [44] C.A. Schuh, T.C. Hufnagel, U. Ramamurty, Overview no.144 — mechanical behavior of amorphous alloys, *Acta Mater.* 55 (2007) 4067–4109.
- [45] H. Huang, H. Zhao, Indenter geometry affecting indentation behaviors of the Zr-based bulk metallic glass, *Mater. Trans.* 55 (2014) 1400–1404.
- [46] R. Maass, J.F. Löffler, Shear-band dynamics in metallic glasses, *Adv. Funct. Mater.* 25 (2015) 2353–2368.
- [47] H. Huang, H.W. Zhao, Z.Y. Zhang, Z.J. Yang, Z.C. Ma, Influences of sample preparation on nanoindentation behavior of a Zr-based bulk metallic glass, *Materials* 5 (2012) 1033–1039.
- [48] H. Bei, Z.P. Lu, E.P. George, Theoretical strength and the onset of plasticity in bulk metallic glasses investigated by nanoindentation with a spherical indenter, *Phys. Rev. Lett.* 93 (2004) 125504.